Microporous and Mesoporous Materials xxx (2018) xxx-xxx

Contents lists available at ScienceDirect

Microporous and Mesoporous Materials

journal homepage: www.elsevier.com

Chemical trapping of gaseous H_2S at high and low partial pressures by an iron complex immobilized inside the montmorillonite interlayer

Daniele Malferrari[a], Elena Castellini[a, *], Fabrizio Bernini[a], Aida Serrano Rubio[b, c], German Rafael Castro[b, c], Claro Ignacio Sainz-Díaz[d], Matteo Caleffi[a], Maria Franca Brigatti[a], Marco Borsari[a]

[a] Department of Chemical and Geological Sciences, University of Modena and Reggio Emilia, Via Campi 103, I-41125 Modena, Italy
[b] SpLine, Spanish CRG BM25 Beamline at the ESRF, 6 Jules Horowitz, F-38043 Grenoble, France
[c] Instituto de Ciencia de Materiales de Madrid (ICMM), CSIC, Sor Juana Inés de la Cruz 3, E-28049 Madrid, Spain
[d] Instituto Andaluz de Ciencias de la Tierra (IACT) CSIC, Universidad de Granada, Av. de Las Palmeras 4, 18100 Granada, Spain

ARTICLE INFO

Keywords:
Hydrogen sulphide
Gas trapping
Montmorillonite
Iron
Hybrid material

ABSTRACT

A stable hybrid material (Mt-Fe(III)Phen) formed by intercalation of the μ-oxo Fe(III)-phenanthroline complex $[(OH_2)_3(Phen)FeOFe(Phen)(OH_2)_3]^{4+}$ (Fe(III)Phen) in montmorillonite (Mt) is able to immobilize H_2S in gaseous phase with high efficiency even at extremely low pressures. DR UV–vis and I.R. spectroscopies, elemental analysis, X-ray powder diffraction, thermal analysis coupled with evolved gas mass spectrometry, and X-ray absorption spectroscopy show that the material has high adsorption capacity, performs fast H_2S trapping and is long-lasting. Moreover, even extremely low levels of H_2S can be removed easily and quickly from gaseous phase using a suitable amount of the trapping material. The immobilization mechanism likely involves a redox reaction between iron (III) and one S^{2-} ion, followed by the binding of a second S^{2-} ion to the metal centre. The process takes place at room temperature, is reversible for several cycles, and does not require pre-treatment of neither gaseous H_2S nor the adsorbent material. Therefore, this modified montmorillonite is a promising material to get rid of H_2S in processes of environmental interest and to obtain gaseous (and gasifiable) high quality hydrocarbons in fuels refineries.

Abbreviations

Mt	Montmorillonite STx-1a
Phen	1,10-phenanthroline ($C_{12}H_8N_2$)
Fe(III)Phen	$[(OH_2)_3(Phen)FeOFe(Phen)(OH_2)_3]^{+4}$
Mt-Fe(III)Phen	solid hybrid material made by montmorillonite STx-1a intercalated with Fe(III)Phen complex in saturation conditions
Mt-FePhen-H_2S	Mt-Fe(III)Phen exposed to H_2S gas

1. Introduction

Sulphur-containing compounds, such as H_2S and thiols, are commonly found in most hydrogen rich gaseous fuels including natural gas, associated petroleum gas, bio-gas, landfill gas, synthesis gas, and coke-oven gas. Removal of H_2S is an obliged process in industry because H_2S is toxic, even low amounts of it are highly corrosive for the refinery equipment and transport lines, and lead to poisoning of many catalysts. Furthermore, H_2S (oxidized to SO_2) originates acid rains and is disliked in all private and public environments because of its bad smell [1]. H_2S therefore represents a serious problem for people living or working close to industrial plants [2]. Several technologies are available for H_2S removal from industrial waste gas streams which can be grouped into several main classes. A first group of technologies involves the multi-step Claus process [3,4], a highly energy intensive industrial procedure which converts H_2S into elemental sulphur through two process steps, *i.e.*, a thermal step (at temperatures above 850 °C) and a catalytic step (using activated aluminium(III) or titanium(IV)oxides). A second group includes chemical treatments in aqueous solutions. These processes can be divided into two categories: those based on oxidation of S^{2-} to S^0, by using iron-chelated solutions, and those involving the trapping of S^{2-} through precipitation of its metallic salts [5]. A third group impli-

* Corresponding author. Department of Chemical and Geological Sciences, University of Modena and Reggio Emilia, Via Campi, 103, 41125 Modena, Italy.
Email address: elena.castellini@unimore.it (E. Castellini)

https://doi.org/10.1016/j.micromeso.2018.01.017
Received 25 October 2017; Received in revised form 15 December 2017; Accepted 12 January 2018
Available online xxx
1387-1811/

cates adsorption on solid adsorbents at various pressures and temperatures. Subcategories of these processes are defined by adsorbent type e.g., oxides such as FeO, ZnO, CuO, MnO, TiO_2, Al_2O_3, Au (110), Ag (111), GaAs (001), ZrO_2 (110) and ceria (110) crystal surfaces; graphene-nanotube hybrid structures, activated carbons and doped activated carbons [6–11]. A forth group, mostly suitable for H_2S removal from biogas, exploits biofiltration [12]. Biofiltration is performed in a multi-phase system in which the contaminated gas is dissolved and adsorbed on a biofilm and then degraded by microorganisms that are immobilized on a packing material forming a thin layer (biofilm). The packing material in the biofilter may be either natural or synthetic and must fulfil the requirements of high surface area, high permeability, and high adsorption capacity [13–15]. A fifth group of technologies consists of adsorption on silica gels, adsorbent rocks (e.g., moisturized pumices, dolomite and limestones) and minerals (e.g., zeolites, clays and maghemite) [16–19].

Recently, Ozekmekci et al. [20] summarized experimental and theoretical reports for removal of H_2S by using zeolites. They concluded that the best results in terms of selectivity were obtained with zeolites with faujasite-like structures, whereas synthetic zeolite-A and ZSM-5 type structures did not performed well. However, Bülow [21] replied that studies of sorption of binary H_2S–CO_2 gas mixtures on zeolites (zeolite-A and faujasite) demonstrated a dual function of these materials. These zeolites may act as both selective sorbents and catalysts for converting H_2S and CO_2 into COS and H_2O, according to the reaction $H_2S + CO_2 \leftrightarrows COS + H_2O$. Eventually, zeolite-A, due to its large specific surface area, reduces the carbonyl sulfide content [22].

In this work we propose an innovative and efficient method for H_2S capture in gaseous phase working even at extremely low pressures using the layer silicate montmorillonite (Mt) intercalated with a μ-oxo Fe(III) phenanthroline complex $[(OH_2)_3(Phen)FeOFe(Phen)(OH_2)_3]^{4+}$, Fe(III)Phen hereafter [23]. Moreover, we review the recent literature on the H_2S capture mechanism and removal performance of swelling clays. Montmorillonite is a 2:1 layer aluminosilicate, in which one sheet of octahedrally coordinated cations (M) is sandwiched between two sheets of tetrahedrally coordinated cations (T) to form a TMT layer. Isomorphic substitutions, mostly in the M sites (e.g., Mg^{2+} and Fe^{2+} for Al^{3+}), induce a permanent negative layer charge, which is compensated by the presence of hydrated cations in the interlayer. Hydroxyl groups complete the coordination of each octahedron. Most of the technological uses of smectite are related to reactions taking place in the interlayer space where the hydrated cations can be easily exchanged [24].

The proposed trapping material (Mt-Fe(III)Phen), which proved to be effective in adsorbing thiols [25], is able to immobilize gaseous H_2S through a redox process involving the oxidation of S^{2-} to S^0 and a subsequent formation of covalent bond between another S^{2-} and the iron centre, providing an efficient and strong retention. In this work, the trapping capacity of this material was determined along with the chemical speciation of the absorbent and adsorbate after interaction. We also demonstrated that the process is reversible: the adsorbent can be easily regenerated and reused several times before exhaustion. In addition, since many civil and industrial contexts produce very low, but prolonged, emissions of gaseous H_2S resulting in latent dangerous accumulation in the environment, specific attention was paid to the exploitation of Mt-Fe(III)Phen as a long-lasting trap immobilizing H_2S also at extremely low levels. This fact, together with a high capacity and rate of H_2S trapping, makes the proposed modified montmorillonite a promising material for applications in industrial and environmental field and for the treatment of the fossil fuels. In addition, although innovative materials demonstrated to selectively adsorb thiols from an H_2S containing gas stream [26,27], for some applicative contexts, like the treatment of fossil fuels or the treatment of gaseous emissions from waste landfills and composting plants, the possibility to simultaneously (and economically) remove all these sulphur compounds even at very low levels results a priority need.

2. Experimental

2.1. Materials

Montmorillonite used in this work is STx-1a (Mt), a source clay from the County of Gonzales, State of Texas, USA, provided by the Clay Minerals Society (The Clay Minerals Society, Source Clays Repository, University of Missouri, Columbia, MO). Mt characterization is reported on the Clay Minerals Society web-page (http://www.clays.org/Sourceclays.html).

$Fe_2(SO_4)_3{\cdot}8H_2O$, acetic acid and NaOH pellets (>99% purity) are Carlo Erba products. 1,10-Phenanthroline ($C_{12}H_8N_2$, Phen), ferroin $Fe(II)Phen_3SO_4$ (>99% purity) are purchased by Sigma-Aldrich. H_2S is supplied by Alpha gas, Air Liquide.

Details of material preparation, already reported in previous works [23,25], are extensively described in SM1. Final adsorbent material, Mt-Fe(III)Phen, is Mt saturated in Fe(III)Phen complex, *i.e.* it contains equivalents of complex which are the double with respect to the CEC of Mt. As already found for other iron-pillared montmorillonite, the exceeding positive charge is neutralized by anions, sulphate in our case [23,28]. The separated solid was washed several times with distilled water to remove residual Fe(III)Phen and dried at 30 °C. This was exactly the material used for investigating the H_2S immobilization.

Reference compounds for X-ray Absorption Spectroscopy (XAS) measurements were: $Fe_2(SO_4)_3{\cdot}8H_2O$, ferroin (see above), $FeSO_4{\cdot}7H_2O$ (Carlo Erba, RPE), and the minerals hematite (Fe_2O_3), pyrite (FeS_2), and magnetite ($FeOFe_2O_3$) are used as reference.

2.2. Immobilization of H_2S on Mt-Fe(III)Phen

The immobilization of H_2S on Mt-Fe(III)Phen yields the samples hereafter indicated as Mt-FePhen-H_2S. The reaction was performed in a glass box covered by a layer of aluminium foil. 100 mg of Mt-Fe(III)Phen is dispersed on the bottom of a 5 cm-diameter glass Petri dish. The glass box hosts an inner and outer gas hose. The gas supplied to the glass box is a mixture of H_2S/Ar whose composition was accurately tuned by means of calibrated mass flow controllers (Alltech Digital Flow Check-HR) and gas mixing valves. The flow was set as to yield a constant partial pressure of H_2S of 250 Pa. Adsorption tests were performed at different times (i.e., from 1 to 166 h). The corresponding S content of the Mt-Fe(III)Phen samples was determined by elemental analysis (Carlo Erba Model 1106 Elemental Analyser).

In the recovery experiments, the Mt-FePhen-H_2S samples were heated at 210 or 295 °C for about 30 min before undergoing each cycle of adsorption/desorption. This time ensures the complete desorption of the adsorbed H_2S. Elemental analyses were performed before and after each thermal cycle.

2.2.1. Immobilization performance at extremely low H_2S pressures

Additional experiments were specifically addressed to investigate the lowest limit value of H_2S vapour pressure for which Mt-Fe(III)Phen is still efficient as a gas trap. The selected values of vapour pressure were 10, 5, 1, 0.3 and 0.15 Pa. These values are not reliable using the calibrated mass flow controller. For this reason, H_2S was produced *in situ* by evaporation of proper volumes of water saturated with H_2S inside a closed glass box (Volume = 1 dm^3; H_2S solubility in water: 4 g dm^{-3} [29]; volumes: 34.38, 17.19, 3.44, 1.03, 0.52 μL for vapour pressure 10, 5, 1, 0.3, 0.15 Pa, respectively; Gilson mod. Pipetman P200 and Gilson mod. Pipetman P20 pipettes were used). The immobilization of H_2S at extremely low levels on Mt-Fe(III)Phen was performed at room temperature (T = 298 K) in a glass box of 1 dm^3 of volume covered by a layer of aluminium foil; different amounts of Mt-Fe(III)Phen (10, 20 and 50 mg) in a glass Petri dish (Φ = 10 cm) and a

proper volume of H_2S saturated water in a small beaker were placed inside the glass box. Exposure time ranged between 0.1 and 100 h.

2.3. Methods

UV–Vis and diffuse-reflectance (DR) UV–Vis measurements were carried out on a UV–Vis spectrophotometer Jasco Instrument mod. V-570. For the solid samples (Mt-Fe(III)Phen and Mt-FePhen-H_2S) the spectrophotometer was equipped with an integrating sphere attachment (Jasco model ISN-470) using Mt as the reference. The elemental analyses (C, N, S) on the samples were performed using a Carlo Erba Elemental Analyser (Model 1106). FT-IR spectra were collected using a JASCO FT/IR 4700 spectrophotometer (resolution: 0.4 cm^{-1}) on KBr pellets. Thermogravimetric analyses (TGA) were performed from Seiko SSC 5200 thermal analyser equipped with a quadrupole mass spectrometer (ESS, GeneSysQuadstar 422) which enables the analysis of gas phases evolved during the thermal reactions (mass spectrometry evolved gas analysis, MS-EGA). Gas sampling by the spectrometer was made using an inert, fused silicon capillary system, heated to prevent gases condensing. Gas analyses was carried out in Multiple Ion Detection mode (MID) to determine the nature of the evolved chemical species with temperature (or time). Background subtraction was applied to obtain the point zero conditions before starting MID analysis. Measurements are performed under the following experimental conditions: heating rate: 20.0 °C/min; heating range: 25–1150 °C; data measurement: every 0.5 s; purging gas: ultrapure helium, flow rate: 100 μL/min. Mass analyses were carried out in multiple ion detection mode measuring the m/z ratios (17 and 18 for H_2O; 28 and 44 for CO_2; 30 for NO and NO_2; 33 and 34 for H_2S; 46 for NO_2; 48, 64, and 66 for SO_2); SEM and FARADAY detector at 1100 V were employed with 1 s of integration time on each measured mass. To avoid differences in relative humidity, samples were equilibrated for 15 min inside the oven using a 100 μL/min flow of ultrapure helium.

X-ray powder diffraction patterns (XRPD) for Mt-Fe(III)Phen and Mt-FePhen-H_2S were recorded from oriented mounts on air-dried samples using a Philips X'Pert PRO diffractometer equipped with X'Celerator detector (CuK-α radiation, 40 kV and 40 mA; $4 \leq 2\theta \leq 20°$, quartz as calibrating standard).

Fe *K*-edge XAS spectra were collected at ESRF European Synchrotron Radiation Facility (Grenoble, France) on the Spanish Beam Line (SpLine, BM25 Branch A). The storage ring was running in uniform mode conditions and working in the current range 180–200 mA. A Si(111) double-crystal monochromator was used, providing an energy resolution of $\Delta E/E \sim 0.41.4 \times 10^{-4}$ eV. For all spectra, a metallic Fe reference foil was used to provide an energy calibration for the monochromator (energy reproducibility: ± 0.05 eV). Data were collected both in transmission and in fluorescence mode at room conditions on about 10 mg of powdered samples mounted between two layer of adhesive Kapton film. The spectra were recorded over a full energy range of 800 eV across the Fe absorption *K*-edge with 0.5 $Å^{-1}$ energy step in the X-ray Absorption Near-Edge Structure (XANES) region (7080–7160 eV) and 0.03 eV in the Extended X-ray Absorption Fine Structure (EXAFS) region up to 15 $Å^{-1}$. The pure grade reagents $Fe_2(SO_4)_3 \cdot nH_2O$, $[Fe(o\text{-phen})_3]SO_4$ (Ferroin), and $FeSO_4$and the minerals hematite (Fe_2O_3), pyrite (FeS_2), and magnetite ($FeOFe_2O_3$) were used as reference. Data reduction and analysis were performed using IFFEFIT software (Athena/Artemis interface) [30,31]. The XAS regions of the spectra were normalized in absorbance using a Victoreen function for atomic absorption basing on the average absorption coefficient.

3. Results

3.1. DR UV–Vis measurements

The interaction of Mt-Fe(III)Phen with H_2S results in a fast and intense chromatic effect, the colour changing from yellow ochre to a very intense ruby red colour (Fig. SM1). Accordingly, the UV–Vis spectrum of Mt-Fe(III)Phen (Fig. 1) displays major changes. In particular, the final spectrum is very similar to that of the $[Fe(II)Phen_3]^{+2}$ complex in solution [23]. More in detail, when Mt-Fe(III)Phen interacts with H_2S, the band at λ = 374 nm, related to the O^{2-}(bridge) → Fe(III) charge-transfer transition and typical of the μ-oxo ferric complexes [32] decreases in intensity. This is paralleled by the increase of a strong band at λ = 520 nm, due to a d→π* metal-to-ligand charge transfer band of $[Fe(II)Phen_n]^{+2}$ type complex [33], that indicates Fe(III) to Fe(II) reduction.

3.2. FT-IR

Exposure of Mt-Fe(III)Phen to H_2S (Mt-FePhen-H_2S spectrum) causes only a slight shift of the phenanthroline bands (i.e., at: 1585, 1520, 1493, 1427, 872, 724 cm^{-1}) which in Mt-Fe(III)Phen occur at 1588, 1522, 1496, 1429, 871, 722 cm^{-1}, leaving the bands corresponding to Mt unchanged (SM2 and Fig. SM2) [25]. According to Schilt [34], these slight shifts are related to Fe(III) to Fe(II) reduction.

3.3. Elemental analysis

The interaction of H_2S with Mt-Fe(III)Phen can be assessed by measuring the change in C, N and S content with time. The S amount strongly increases with the interaction time (Fig. 2a). S is already present in Mt-Fe(III)Phen prior to exposure to H_2S as SO_4^{2-} ions are co-adsorbed with Fe(III)Phen when Mt is saturated with the complex [23]. Fig. 2a shows the time course of the S content (data purged from the S content due to the SO_4^{2-} ions) inside Mt-Fe(III)Phen. It shows that the process takes place into at least two distinct steps. The first step (with a duration of about 20 h) is initially fast (first 4 h), then slows down and corresponds to approximately 34% of the maximum amount of S that can be immobilized inside Mt. The second step can be considered fully completed after 75 h. Eventually, the S content remains constant (up to 220 h). The S/Fe molar ratio of the first step is approximately 0.5,

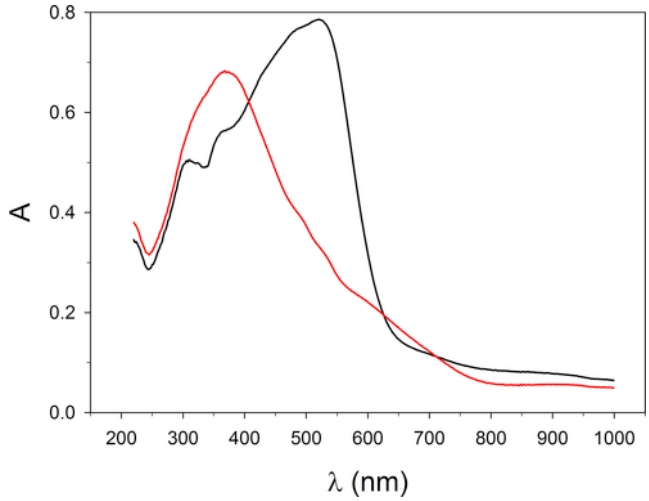

Fig. 1. DR UV–Vis spectra of Mt-Fe(III)Phen before (red line) and after 5 h of interaction with H_2S (black line). (For interpretation of the references to colour in this figure legend, the reader is referred to the Web version of this article.)

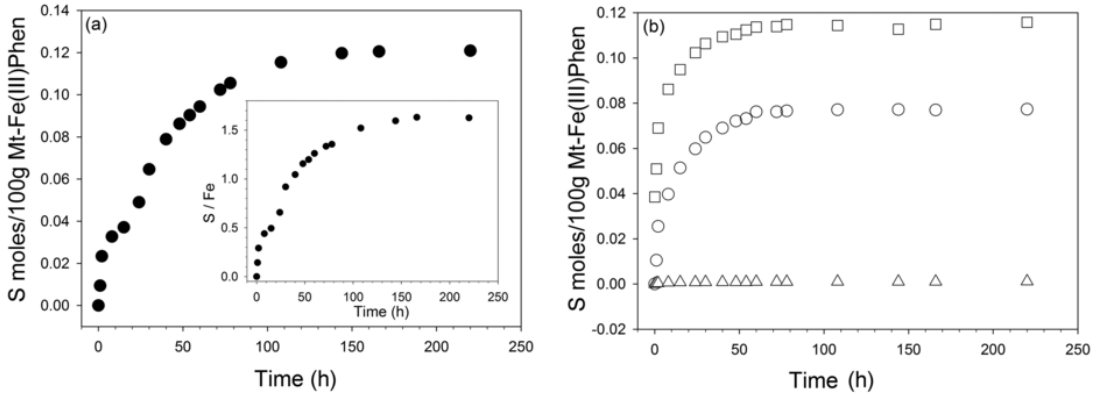

Fig. 2. (a) H_2S adsorption (S moles/100 g Mt-Fe(III)Phen) *vs.* time for pristine Mt-Fe(III)Phen. The inset plots the S/Fe molar ratio *vs.* time. (b) H_2S adsorption (S moles/100 g Mt-Fe(III)Phen) *vs.* time for the hybrid material after one cycle of desorption at 210 (square), 295 (circle), and 400 °C (triangle). Data purged from the S content due to SO_4^{2-} present in Mt-Fe(III)Phen.

while that corresponding to the limit value of the S content is about 1.5 (Fig. 2a, inset).

3.4. X-ray powder diffraction

At room temperature, the Mt layer periodicity increases from $d_{001} = 15.3$ Å to $d_{001} = 18.0$ Å when the mineral is intercalated with Fe(III)Phen complex in saturation conditions [23]. The XRPD patterns of Mt-FePhen-H_2S are very similar to those of Mt-Fe(III)Phen (Fig. SM3). This suggests that the S-derivatives immobilized inside the interlayer occupy the empty areas created by the intercalation of the complex which is able to superimpose a channel structure to the interlayer [23].

3.5. TGA and MS-EGA

Fig. 3 compares thermogravimetric (TGA) curve and its first derivative (DTGA) for both Mt-Fe(III)Phen [23] and Mt-FePhen-H_2S. The nature of the gases produced by the thermal reactions was determined by MS-EGA analysis (Fig. 4). The TGA and DTG curves of Mt-FePhen-H_2S show: *i)* in the thermal range 25–100 °C a noticeable effect at about 55 °C that is related to H_2O loss as shown by MS−EGA curves (Fig. 4, H_2O release, m/z = 18): the mass loss associated to this reaction is about 4.0%; *ii)* two strong and well-defined reactions at 210 and 295 °C associated to a remarkable mass loss of about 10%. These reactions are not observed for untreated Mt-Fe(III)Phen and can be confidently related to effects associated to the immobilization of H_2S in Mt-Fe(III)Phen. MS−EGA curves indicate a contemporary release of H_2O (m/z = 18), H_2S (m/z = 34), and SO_2 (m/z = 64) at 210 °C (mass loss ≈6.8%) and of H_2O and SO_2 at 295 °C (mass loss ≈3.2%); *iii)* in the thermal range between 400 and 1150 °C several different effects occur yielding maxima at 497, 625, 779, and about 942 °C (broad), and resulting in an overall mass loss of 15.65%. These effects are associated to a concomitant CO_2 and NO_x release and are similar to those already observed for Mt-Fe(III)Phen (Fig. 4). Therefore they can be attributed to thermal decomposition of the immobilized iron complex and dehydroxylation of Mt [23]. The comparison between the thermal behaviour of Mt-FePhen-H_2S and Mt-Fe(III)Phen shows that the main changes occur in the temperature range between 210 and 295 °C. Thermal effects below 100 °C and in the thermal range between 400 and 1150 °C are similar for Mt-Fe(III)Phen and Mt-FePhen-H_2S.

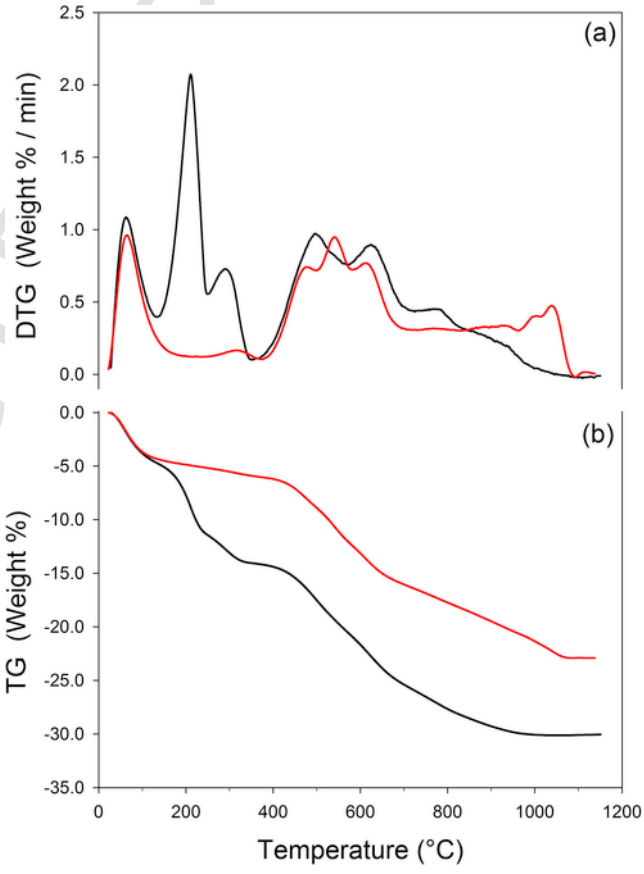

Fig. 3. Comparison between the DTG (a) and TG (b) curves of Mt-Fe(III)Phen (red lines) and Mt-FePhen-H_2S (black lines). (For interpretation of the references to colour in this figure legend, the reader is referred to the Web version of this article.)

3.6. X-ray absorption spectroscopy

X-ray Absorption Spectroscopy (XAS) studies at the Fe *K*-edge were focused on both X-ray Absorption Near Edge Structure (XANES) and Extended X-ray Absorption Fine Structure (EXAFS) signals, which provide information on iron speciation and the local structural environment of Fe ions. In particular, in XANES region several features can be distinguished: a pre-edge region attributed to the 1s → 3d transition, the shoulder on the absorption edge that corresponds to the forbidden

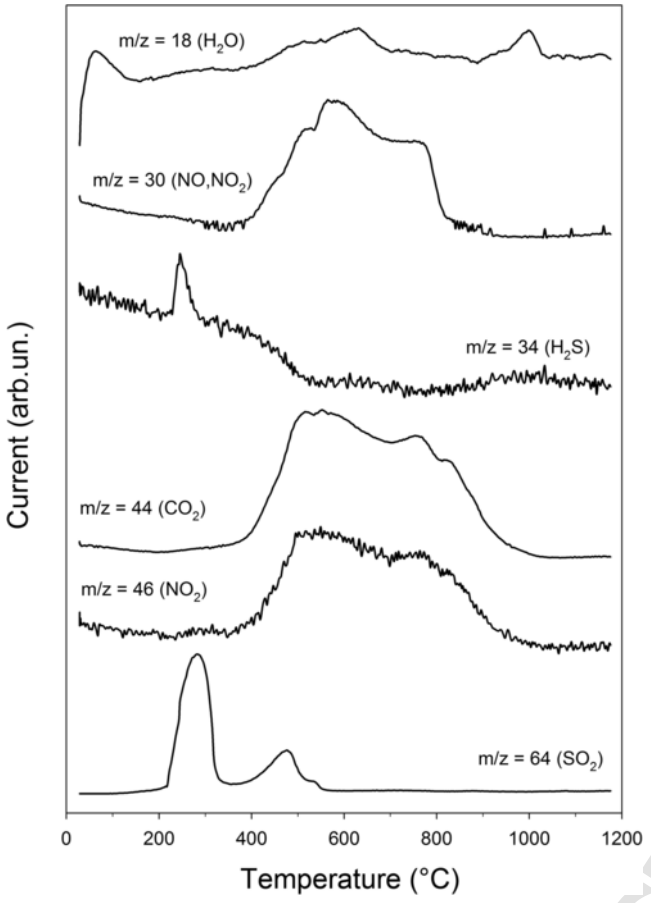

Fig. 4. Mass analysis of the evolved gases as a function of temperature for Mt-FePhen-H_2S recorded at m/z = 18 (H_2O), 30 (NO and NO_2), 34 (H_2S), 44 (CO_2), 46 (NO_2), and 64 (SO_2).

transition 1*s* → 4s and the energy of main peak produced by a 1s → 4p electron transition [35]. Clear variations of these features are observed with changes in Fe oxidation state and local structure, including energy shifts of the main absorption, and changes in the intensity, shape, and centroid of the pre-edge feature.

Fig. 5a compares XANES spectrum of Mt-FePhen-H_2S with those of Mt-Fe(III)Phen, α-Fe_2O_3 (the mineral hematite) and Fe(III)Phen complex [36], the last two selected as the reference compounds. The energy values of absorption edges associated with 1s→4p transitions are similar in Mt-Fe(III)Phen and in the selected reference compounds where iron is in the trivalent form. Remarkable differences can be observed when comparing the reference compounds with the Mt-FePhen-H_2S XANES spectrum: a clear shift towards lower energies is noted at the absorption edge, the white-line, and the pre-peak position, indicating Fe(III) reduction. Fig. 5b compares the XANES spectrum for Mt-FePhen-H_2S with those of the reference compounds $FeSO_4$, $[Fe(o\text{-}Phen)_3]SO_4$ (pure grade reagents), and the mineral pyrite (FeS_2) in which iron is present as Fe(II). Clear differences can be noted in the XANES curves. However, no changes are observed in the energy position at the absorption edge and at pre-peak centroid of XANES spectrum for Mt-FePhen-H_2S and references, indicating that the oxidation state of iron is the same.

The absorption edge position of XANES spectra shifts with the oxidation state of the Fe ion. This correlation is known as Kunzl's law and represents an empirical law which helps in estimating the oxidation state of transition metals ions [37,38]. The linear relationship obtained from reference commercial compounds between the position at the energy edge and the oxidation state was found to be E_{pe} = 7112.1(7) + 4.1(3) *OS*, as depicted in Fig. 6a. This expression and the absorption edge position for Mt-FePhen-H_2S yields an iron oxidation state of 2.4(3). On the other hand, pre-peak at the *K*-absorption edge spectrum of transition metals can be also related to their oxidation state [39]. As for the absorption edge, we found a linear correlation E_{pe} = 7109.8(5) + 1.7(2) *OS* between the pre-edge centroid position and the Fe oxidation state for the references (Fig. 6b). From such correlation the oxidation state of Mt-FePhen-H_2S was determined to be 2.3(6). These results are in agreement with that obtained by applying the Kunzl's law to absorption edge position. Table 1 reports the calculated values for the oxidation state of Mt-Fe(III)Phen, Fe(III)Phen complex, and Mt-FePhen-H_2S, by using Kunzl's law and the pre-peak centroid position. Although these measurements are not quantitative, this analysis confirms a large reduction of trivalent iron in Mt-Fe(III)Phen upon interaction with H_2S, in agreement with the DR UV–Vis measurements.

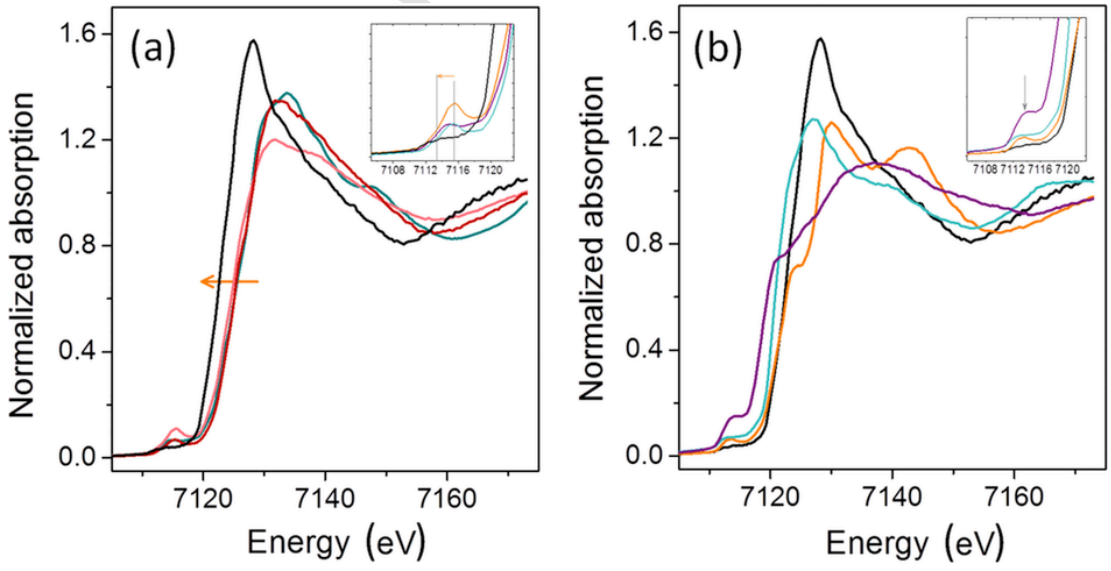

Fig. 5. XANES spectrum of Mt-FePhen-H_2S (black line) compared with the spectra of: (a) Mt-Fe(III)Phen (red line), hematite α-Fe_2O_3 (dark-cyan line), and Fe(III)Phen complex (pink line); (b) $[Fe(o\text{-}Phen)_3]SO_4$ (orange line), $FeSO_4$ (cyan line), and pyrite FeS_2 (purple line). A magnification of the pre-edge region is also provided. (For interpretation of the references to colour in this figure legend, the reader is referred to the Web version of this article.)

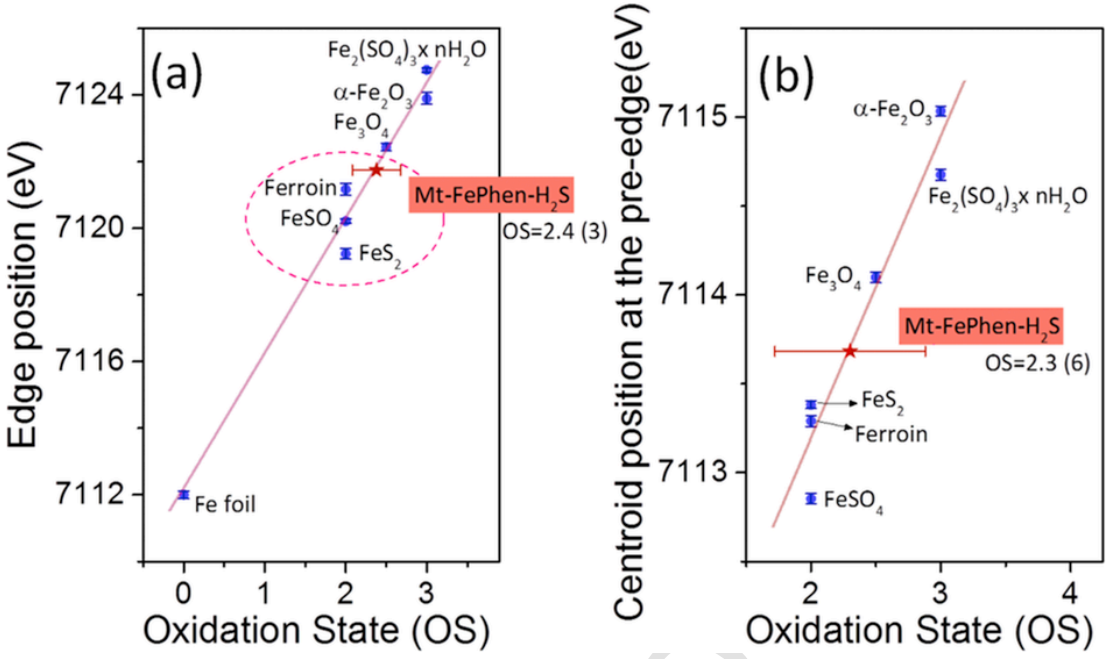

Fig. 6. Linear relationship between (a) position at Fe *K* absorption edge and (b) pre-peak centroid position and oxidation state for reference commercial compounds (blue circles). Oxidation state for sample Mt-FePhen-H_2S (red star) is calculated from each approach and depicted in each figure. (For interpretation of the references to colour in this figure legend, the reader is referred to the Web version of this article.)

Table 1
Oxidation state of samples from absorption edge (Kunzl's law) and pre-peak centroid positions.

Sample	Absorption edge position (Kunzl's law)		Pre-peak centroid positions	
	Absorption edge position (eV)	Oxidation state	Absorption edge position (eV)	Oxidation state
Fe(III)Phen complex	7123.7 ± 0.2	2.9 ± 0.4	7115.25 ± 0.03	3.2 ± 0.7
Mt-Fe(III)Phen	7124.4 ± 0.2	3.0 ± 0.4	7115.27 ± 0.03	3.2 ± 0.7
Mt-FePhen-H_2S	7121.7 ± 0.3	2.4 ± 0.3	7113.68 ± 0.05	2.3 ± 0.6

3.7. Regeneration performance

Mt-FePhen-H_2S was subjected to thermal treatment at 210 and 295 °C. This allows information to be gained on the thermal desorption of immobilized H_2S as the above two temperatures correspond to the well-defined peaks in DTG curves associated to the emission of S-derivatives (H_2S and SO_2). After about 10 min at 295 °C, the S content in 1 g sample decreases from 5.05% to the pristine 1.18%, i.e. to the value observed for Mt-Fe(III)Phen before treatment with H_2S and associated to structural SO_4^{2-} ions intercalated in Mt together with Fe(III)Phen [23].

Treatment at 210 °C yields a decrease in S content to 2.41% after about 2 min, without further changes. Hence, in these conditions, the release of immobilized S is incomplete. In both cases, however, the thermal treatments are reversible for at least 20 cycles and, under exposure to H_2S, the same increase in the amount of entrapped S is observed, corresponding to about 2/3 of the maximum amount of S obtained starting from fresh Mt-Fe(III)Phen (Fig. 2b). No changes in the IR spectra occur. Thermal treatment at $T \geq 400$ °C induces irreversible desorption and hampers any eventual H_2S immobilization (Fig. 2b). In addition, dramatic changes in the IR spectra of the exposed material occur, in agreement with the observation that at temperature higher than 400 °C the ligand phenanthroline undergoes thermal decomposition [23].

3.8. Immobilization performance at extremely low H_2S levels

The amounts of H_2S immobilized by Mt-Fe(III)Phen at extremely low levels of H_2S (corresponding to partial pressures of 10, 5, 1 and 0.3 Pa) were determined by elemental analysis at different exposure times (Fig. 7, Figs. SM4, SM5) and Mt-Fe(III)Phen amount (Figs. SM6, SM7). As found at higher H_2S partial pressure, evident and fast chromatic effects occur (from yellow ochre to ruby red colour, Fig. SM8) as well as remarkable changes in the DR UV–Vis spectrum (appearance of a composite strong band at $\lambda = 520$ nm, Fig. SM9). Therefore, it is conceivable that the immobilization process at low pressure is the same as that occurring at higher pressure. The data of Fig. 7, SM4, SM5 show that the amount of immobilized H_2S increases with time in a bimodal fashion: the process is initially fast (1–4 h), then it becomes much slower. In addition, at constant immobilization times, also the amount of Mt-Fe(III)Phen increases the trapping efficiency (Figs. SM6, SM7), yielding an almost complete removal of H_2S even for short times.

4. Discussion

4.1. Sulphur immobilization and desorption

The storage of H_2S inside the interlayer of Mt-Fe(III)Phen is a complex process that involves at least two steps and two different S species. In fact, spectroscopic data (DR UV–Vis and XANES spectra) indicate that, upon the exposure to H_2S, Fe(III) undergoes reduction to Fe(II)

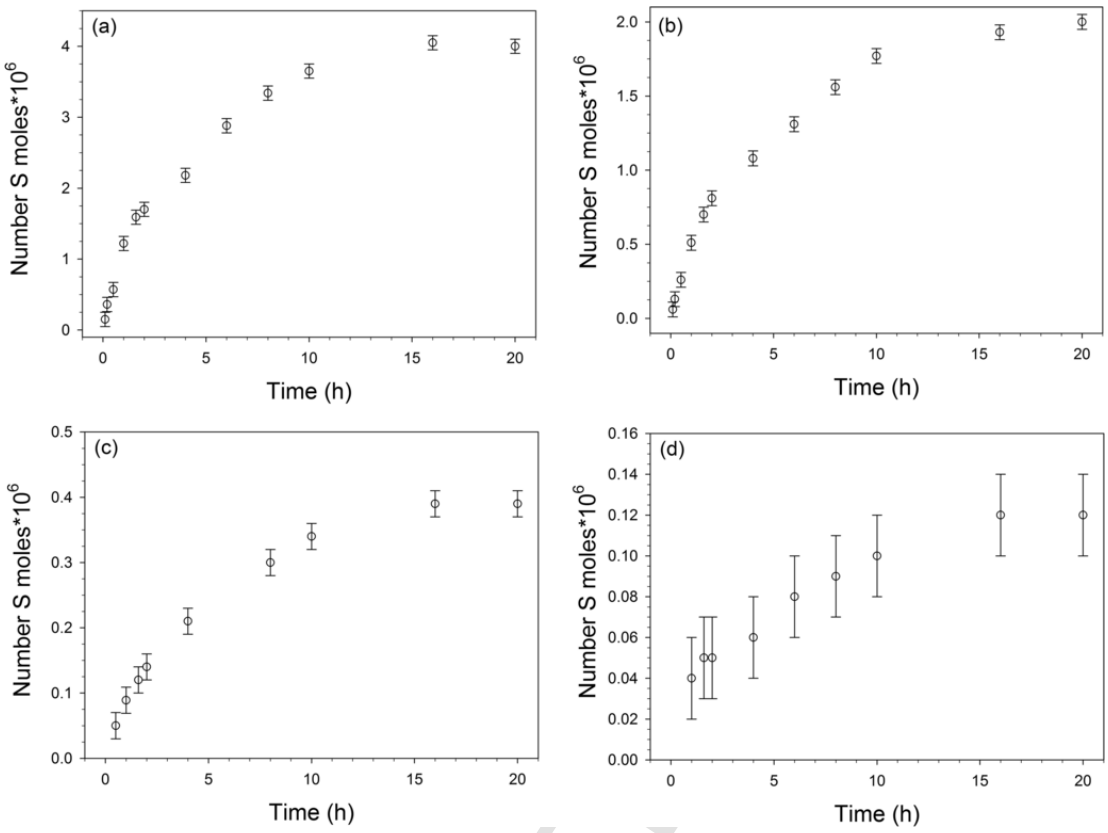

Fig. 7. Number of S moles immobilized onto 50 mg of Mt-Fe(III)Phen as a function of time in different conditions of vapour pressure of H_2S inside the glass box: (a) 10 Pa, (b) 5 Pa, (c) 1 Pa, and (d) 0.3 Pa.

and this reaction is reasonably coupled to the oxidation of S^{2-} to S^0. Eventually, the resulting Fe(II) complex (confidently $[Fe(II)Phen]^{2+}$) binds a second S^{2-} ion. A similar process has been previously observed for the interaction of H_2S with Fe_2O_3 [40,41]. Therefore, the immobilization mechanism could be the following:

$$[PhenFe(III)\text{-}O\text{-}Fe(III)Phen]^{4+} + H_2S \rightarrow 2\ [PhenFe(II)]^{2+} + S^0 + H_2O \quad (1)$$

$$2\ [PhenFe(II)]^{2+} + 2H_2S \rightarrow 2\ [PhenFe(II)S] + 4\ H^+ \quad (2)$$

This hypothesis is strengthened by XAS measurements. Fig. 8 displays the modulus of the Fourier transform (FT) of the EXAFS signal for the Mt-FePhen-H_2S sample and the FeS_2 reference. The FT was carried out for the $k^2\ \chi(k)$ weighted EXAFS signal between 2.5 and 10.5 $Å^{-1}$. To make data fitting, the energy shift E_0 measured at the edge point was first calculated for the reference compound FeS_2; after the found value was fixed and employed to refine data for Mt-FePhen-H_2S. For FeS_2, the first intense peak in the FT corresponds to the six sulphur atoms neighbouring the Fe ion. A good fitting was achieved in the first coordination shell in which the interatomic distance is of 2.245(2) Å and the Debye-Waller (DW) factor σ^2 of 0.0033(3).

Fourier transformed amplitude of the EXAFS signal for Mt-FePhen-H_2S shows an intense peak with an interatomic distance corresponding to the first neighbour atoms that is smaller than the Fe-S distance obtained for reference FeS_2. As it was not possible to fit the EXAFS signal for Mt-FePhen-H_2S assuming only sulphur atoms acting as first neighbours around the Fe ion, also atoms other than S must be bound to Fe. Indeed, it is possible to fit the EXAFS spectra for Mt-FePhen-H_2S by considering: *i)* nitrogen atoms as first neighbours approaching the Fe ion with a Fe-N interatomic distance of 2.092(2) Å and a DW factor σ^2 of 0.0062(4) $Å^2$, and *ii)* including sulphur ions as second neighbouring atoms at a distance of 2.14(2) Å, which is slightly larger than the Fe-N

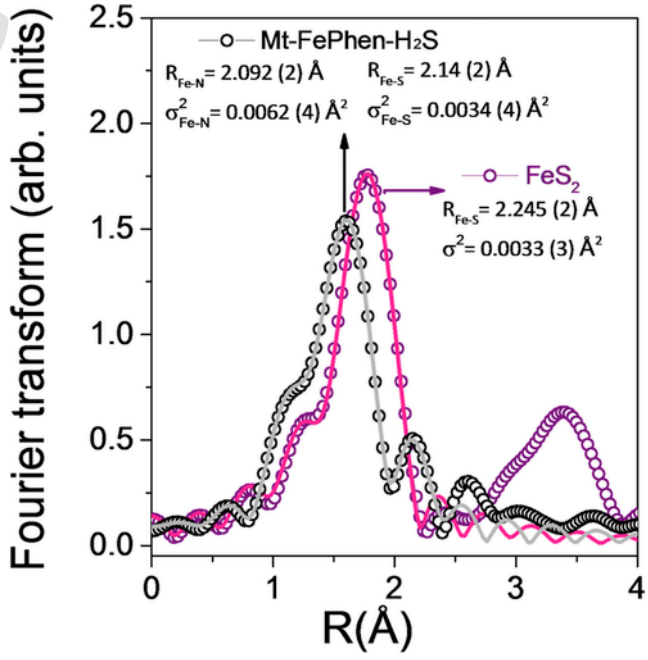

Fig. 8. Modulus of the Fourier Transform (FT) of the EXAFS signal at Fe *K*-edge for Mt-FePhen-H_2S (black circles) and reference FeS_2 (purple circles). Continuous lines represent best-fitting simulations of the first peak. Obtained first neighbours parameters are reported in the figure. (For interpretation of the references to colour in this figure legend, the reader is referred to the Web version of this article.)

distance (included into the first intense peak of the FT of EXAFS signal) and with a DW factor σ^2 of 0.0034(4) Å^2 (Fig. 8). These structural results nicely agree with the second step of the proposed immobilization mechanism (reaction (2)) which involves the binding of S^{2-} to a Fe(II) coordinated by the two N atoms of a phenanthroline ligand.

The presence of two types of sulphur species is indirectly confirmed by the thermal analysis of Mt-FePhen-H_2S. In fact, S-derivatives are observed in the gas produced by the thermal treatment at about 210 and 295 °C, as previously described in paragraph 3.5. This means that the mass ratio is about 2. This result can be interpreted if we assume that at 210 °C the S^{2-} ion bound to Fe(II) is released as H_2S and SO_2, while at 295 °C the S^0 produced in reaction (1) is oxidized to SO_2. The kinetics of interaction of Mt-Fe(III)Phen with H_2S observed for the first step of adsorption is rather fast (Fig. 2a). In particular, in the first 2 h 100 g of Mt-Fe(III)Phen adsorb about 0.32 g H_2S/h. From 180 to 230 °C, desorption of sulphur deriving from H_2S occurs quickly, but only 2/3 of the total amount is released. The resulting solid is formed by Mt intercalated with the $[PhenFe(II)]^{2+}$ complex (in the DR UV–Vis spectra the strong band at $\lambda = 520$ nm, typical of $[PhenFe(II)]^{2+}$, is maintained) which is still able to bind H_2S to restore the starting amount (Fig. 2b). In this temperature range, desorption probably involves only S^{2-} ions bound to Fe(II), but not S^0 resulting from the redox reaction with Fe(III)Phen. From 230 to 380 °C desorption is complete, but the overall process is slower. Indeed, the time requested to desorb 2/3 of S is still fast, but the remaining 1/3 takes longer to desorb. In this temperature range, desorption probably involves both S^{2-} and S^0 located inside the interlayer. The thermal cycles between 180 and 350 °C can be repeated several times (at least 20) without remarkable changes in the kinetics of immobilization. Between 230 and 350 °C, S is entirely removed, but a new exposure to H_2S yields an uptake of only 2/3 of the starting amount of S (Fig. 2b). In fact, under these conditions, each $[PhenFe(II)]^{2+}$ can bind only one S^{2-} ion and no further oxidation of S^{2-} occurs. The immobilization is once again reversible. However, at temperatures above 380–400 °C, desorption is fast, but irreversible and the resulting solid is no more able to interact with H_2S (Fig. 2b). Up to 350 °C the IR spectra of Mt-Fe(III)Phen remain unchanged but the signals of water, suggesting that the thermal treatment does not affect the intercalated complex which is still able to immobilize H_2S. Upon treatment at temperatures higher than 380–400 °C, the IR spectra show strong changes in the bands of the aromatic rings [25], indicative of thermal decomposition of the iron complex, which hampers H_2S immobilization.

The data reported in Fig. 7, SM4, SM5 indicate that Mt-Fe(III)Phen exhibits a strong ability in immobilizing H_2S even at very low partial pressure. As found at higher H_2S pressure, the kinetics of trapping consists of two steps. The former corresponds to about 1/3 of the saturation amount of H_2S and is very fast, while the latter is quite slower (Fig. 7, SM4, SM5). The trapping rate increases with increasing the H_2S partial pressure and Mt-Fe(III)Phen amount. Probably it is affected by a complex diffusion process of H_2S inside the pillared interlayer, perhaps controlled by the accumulation of S^0 and the formation of the bonds between Fe(II) and S^{2-} in the outer regions of the interlayer. Reasonably, these factors becomes more important as the partial pressure of H_2S decreases.

It is apparent that, using a proper amount of trapping materials, the almost complete removal of H_2S can be obtained rapidly (Fig. 9). The extreme sensitivity of Mt-Fe(III)Phen is further confirmed by DR UV–Vis measurements. In fact, also at low partial pressures, the DR UV–Vis spectra show the characteristic composite peak at $\lambda = 520$ nm (Fig. SM9) already after 30 min. At the lowest investigated H_2S partial pressure (0.15 Pa), no immobilized S is detected on Mt-Fe(III)Phen even after a long exposure, probably due to the intrinsic limit of the adopted procedure (elemental analysis). However, the DR UV–Vis spectra show the typical well-shaped composite band at $\lambda = 520$ nm after 30 min,

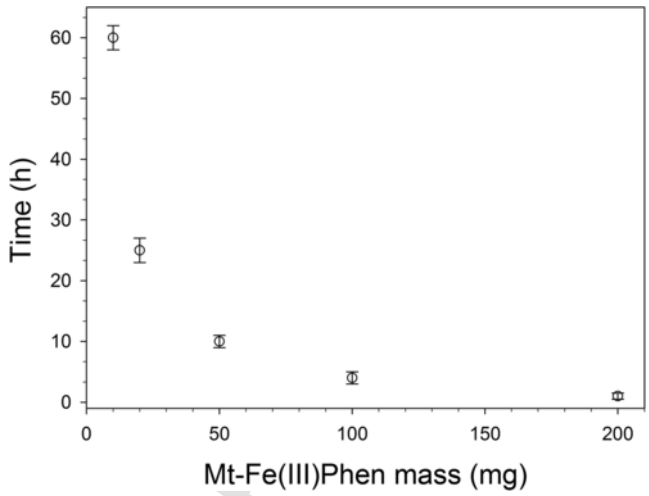

Fig. 9. Time required to remove more than 90% w/w of H_2S at vapour pressure of 10 Pa inside the glass box as a function of the Mt-Fe(III)Phen mass.

suggesting that the reaction between Fe(III)Phen and H_2S on Mt surface still occurs despite the extremely low gas pressure.

4.2. Experimental approaches for H_2S removal by clays

Several materials and various approaches are currently used to remove H_2S from gaseous phases exploiting clay minerals [23]. The procedures are mainly based on chemical linkage or catalytic oxidation and often differ considerably in the adopted physical and chemical conditions. This obstacles a direct comparison among the efficiencies of the different methods.

Modified clays. Stepova et al. [42] used a carbonate-rich montmorillonite modified by iron and copper metal oxides to remove H_2S in low-concentrated exhausted gases. Fe-modified montmorillonite shows significant H_2S removal capacity, although its adsorption capability steadily decreased after each adsorption–regeneration cycle reaching exhaustion after about 20 cycles. Compared to iron-modified montmorillonite, the exhaustion time of copper-modified montmorillonite was distinctly shorter.

Pillared clays are characterized and discussed in various papers [e.g. Refs. [41,43,44]. Nguyen-Thanh and Bandosz [45] investigated Al pillared montmorillonite doped with Fe^{3+}, Zn^{2+}, and Cu^{2+}. The best performing materials, in terms of sulphide adsorption, are those doped with Cu^{2+}, because of its high propensity to form sulphides. In the presence of iron, the removal of hydrogen sulphide is not efficient because of the clustering of iron and the oxidation of H_2S to elemental sulphur first and then to SO_2, which is very weakly adsorbed on the surface. Nguyen-Thanh et al. [46] investigated H_2S removal efficiency of Al-pillared montmorillonite doped with Fe^{3+} and suggested that hydrogen sulphide reacts with Fe^{3+}on the surface of the iron-modified clay. The product of this reaction can be either iron sulphides or SO_2, after catalytic oxidization on iron (hydro)oxides. Subsequent oxidation may lead to sulphate formation. Bineesh and co-worker studied a series of vanadium-doped pillared montmorillonite samples, *i.e.* pillared with Ti [47–49], Zr [49–53], Fe [54] and Al [55], with various amounts of vanadium to evaluate their performance for the selective catalytic oxidation of H_2S. They observed better performances for vanadium-doped pillared clays when compared to pillared clays without vanadium. H_2S conversion over vanadium doped pillared clays increases with increasing vanadium content up to 6–7 wt % in weight. However, it decreases at higher vanadium concentrations due to the decrease of surface area and to the formation of the crystalline V_2O_5 phase. In the presence of water and ammonia using a V-doped Zr pillared montmorillonite, H_2S is converted to ammonium thiosulphate and elemental sulphur [53].

Kim et al. [56] studied the catalytic oxidation of H_2S in the presence of ammonia on niobium pentoxide supported by Fe-pillared clay catalysts and demonstrated that H_2S can be successfully converted to elemental sulphur and ammonium thiosulphate without significant emission of sulphur dioxide. Nb after reacting with H_2S is partially reduced (from 5 + to lower oxidation states).

Light expanded clay aggregates (Leca). KubebaTabase et al. [57] observed enhanced H_2S sorption in Fe_2O_3-rich Leca samples, thus suggesting that Fe_2O_3 in Leca can remove H_2S by chemisorption. Pre-humidification of H_2S was observed to increase the adsorption performance of Leca compared to dry conditions.

Modified kaolin minerals. Louhichi et al. [58] modified a kaolin sample with iron and copper chlorides in order to introduce active centres for H_2S adsorption. On the surface of metal-modified kaolin, H_2S reacts with Cu^{2+} and Fe^{3+} ions to form sulphides or can be catalytically oxidized to SO_2 on Fe(Cu) (hydro) oxides.

In Table 2 data concerning the immobilization of H_2S obtained by selected methods based on H_2S/metal ions interaction are reported together with other info. It is apparent that the different procedures involve considerable variability in the value of the amount of immobilized H_2S and of the metal responsible for the entrapment. The mechanism proposed hereby that excludes catalytic oxidation processes involving O_2, leads to a S/Fe molar ratio equal to 1.5. The values reported in Table 2 are mostly lower or almost equal to 1.5. Higher values are obtained only for pre-humidified Fe-slags, where the high basicity of the slags and the presence of proper amounts of H_2O allows a different catalytic mechanism involving the oxidation of S^{2-} by O_2 [41].

In conclusions, Mt-Fe(III)Phen is able to immobilize a large amount of H_2S, also at very low concentration, in the absence of oxidation processes due to O_2. This property allows the use of the Mt-Fe(III)Phen also in anaerobic environment. In addition, the process is reversible and the adsorbent material can be re-used several times. Mt-Fe(III)Phen is easily prepared from easy-to-find materials and its features are highly reproducible. H_2S immobilization does not require any pre-treatment or grinding/selection processes.

Table 2
Different procedures for H_2S immobilization. NT, no treatment; hum, humidification of the gas before interaction with solid; Y, reversible reaction; P, partially reversible; na, information not available.

Immobilizing Material	Max sulphur sorption mg/g	nS/nMetal (mol/mol)	Metal content (%)	Temperature	Treatment	Type of Process	Reversibility	Reference
Mt-Fe(III)Phen	38.7	1.60	4.21	room	NT	Oxidation to S^0 + bond S^{2-}	Y	This paper
Fe-bentonite	42.9	1.65	4.54	room	NT	bond S^{2-}	P	Stepova 2009 [42]
Cu-bentonite	13.8	0.64	4.28	room	NT	bond S^{2-}	P	Stepova 2009 [42]
Fe-Slag	30	0.33–0.45	11.7–15.7	room	NT	Oxidation to S^0 + bond S^{2-}	na	Montes-Morán 2012 [41]
Fe-Slag	120–180	1.79–2.0	11.7–15.7	room	hum	Oxidation to S^0 + bond S^{2-}	na	Montes-Morán 2012 [41]
Zn-Katalco$_{JM_F}$	6	0.02	~80	300 °C	NT	bond S^{2-}	P	Mureddu 2014[a]
Zn$_{_F}$	10	0.13	~15	300 °C	NT	bond S^{2-}	Y	Mureddu 2014[a]
Fe$_{_F}$	80	1.0	~14	300 °C	NT	Oxidation to S_2^{2-} + bond	P	Mureddu 2014[a]
Al–Mt	0.63	0	0	room	hum	na	na	Nguyen-Thanh 2003 [45]
Fe–Mt	9.65	0.26	6.4	room	hum	Oxidation + bond	na	Nguyen-Thanh 2005 [46]
FeOx–Mt	0.57	< 0.01	20.8	room	hum	Oxidation + bond	na	Nguyen-Thanh 2005 [46]
AlFe–Mt	17.64	0.31	9.82	room	hum	Oxidation + bond	na	Nguyen-Thanh 2003 [45]
AlZn–Mt	20.94	0.91	4.03	room	hum	Oxidation + bond	na	Nguyen-Thanh 2003 [45]
AlCu–Mt	48.77	1.25	7.72	room	hum	Oxidation + bond	na	Nguyen-Thanh 2003 [45]

[a] See Ref. [59].

5. Conclusions

Intercalation of Fe(III)Phen complex inside the interlayer of Mt yields a hybrid material with a significant ability to immobilize H_2S in gas phase. The process takes place easily at room temperature, is reversible and does not require pre-treatment of both gaseous H_2S (i.e. humidification) and the adsorbent material (grinding, size selection). Even extremely low levels of H_2S can be removed easily and quickly from gaseous phases using the proper amount of the trapping materials. In addition, Mt-Fe(III)Phen works well for long. Such long working life has probably to do with the high structuring effect induced in the interlayer by Fe(III)Phen complex. The formation of structured channels probably allows easy diffusion of gaseous H_2S. The redox properties of the iron complex, the high affinity of Fe(II) towards S^{2-} ion and the presence of basic sites able to bind the protons from H_2S inside the interlayer account for the highly sensitive trapping process. The proposed immobilizing mechanism is based on EXAFS structural results which prove that the iron of the hybrid material after H_2S binding is mainly a Fe(II) species, coordinated by nitrogen and sulphur atoms. It is worth noting that the proposed material can find applications in fuels and chemical industries to obtain gaseous (and gasifiable) high quality hydrocarbons.

Acknowledgements

We acknowledge the University of Modena and Reggio Emilia for FAR 2016 funding program (PAsTIME Project).

Appendix A. Supplementary data

Supplementary data related to this article can be found at https://doi.org/10.1016/j.micromeso.2018.01.017.

Additional information on material preparation (SM1); additional figures on materials characterization before and after H_2S interaction (pictures, Fig. SM1; FT-IR measurements, SM2 and Fig. SM2; XRPD measurements, Fig. SM3); additional figures on H_2S adsorption by Mt-Fe(III)Phen at very low pressure levels (as a function of time for a fixed mass, Figs. SM4 and SM5 and as a function of adsorbing mass for a fixed time, Figs SM6 and SM7) and the corresponding pictures (Fig. SM8) and DR-UV-Vis measurements (Fig SM9).

References

[1] A.J. Cramer, J.M. Cole, J. Mater. Chem. A 5 (2017) 10746–10771.
[2] A. González-Sánchez, S. Revah, M.A. Deshusses, Environ. Sci. Technol. 42 (2008) 7398–7404.
[3] A.L. Kohl, R. Nielsen, Gas Purification, fifth ed., Gulf Publ. Co., Houston, TX, 1997.
[4] A. Piéplu, O. Saur, J.-C. Lavalley, O. Legendre, C. Nédez, Sci. Eng. 40 (1998) 409–450.
[5] N. Abatzoglou, S. Boivin, Biofuels, Bioprod. Bioref 3 (2009) 42–71.
[6] D.M. Jaffey, R.J. Madix, Surf. Sci. 258 (1991) 359–375.
[7] G. Lei, C. Liu, H. Xie, J. Liu, Chem. Phys. Lett. 616–617 (2014) 232–236.
[8] Y. Yu, StJ. Dixon-Warren, N. Astle, Chem. Phys. Lett. 312 (1999) 455–460.
[9] O. Voznyy, J.J. Dubowski, J. Phys. Chem. C 112 (2008) 3726–3733.
[10] Y.L. Yang, W.K. Chen, C.H. Lu, Chin. J. Chem. 25 (2009) 1457–1463.
[11] S. Zhao, L. Ling, B. Wang, R. Zhang, D. Li, Q. Wang, J. Wang, J. Phys. Chem. C 119 (2015) 3674–3683.
[12] M. Syed, G. Soreanu, P. Falletta, M. Béland, Can. Biosyst. Eng. 48 (2006) 2.1–2.14.
[13] C. Rattanapan, P. Boonsawang, D. Kantachote, Bioresour. Technol. 100 (2009) 125–130.
[14] R.A.S. Lestari, W.B. Sediawan, S. Syamsiah, Sarto, J.A. Teixeira, J. Environ. Chem. Ecotoxicol. 4 (2016) 2370–2377.
[15] S. Gerrity, C. Kennelly, E. Clifford, G. Collins, Environ. Technol. 37 (2016) 2252–2264.
[16] B. Ozturk, Y. Yildirim, Process Saf. Environ. Protect. 86 (2008) 31–36.
[17] P. Cosoli, M. Ferrone, S. Pricl, M. Fermeglia, Chem. Eng. J. 145 (2008) 86–92.
[18] M. Husmann, C. Zuber, V. Maitz, T. Kienberger, C. Hochenauer, Fuel 181 (2016) 131–138.
[19] G. Huang, E. He, Z. Wang, H. Fan, J. Shangguan, E. Croiset, Z. Chen, Ind. Eng. Chem. Res. 54 (2015) 8469–8478.
[20] M. Ozekmekci, G. Salkic, M. Ferdi Fellah, Fuel Process. Technol. 139 (2015) 49–60.
[21] M. Bülow, Fuel Process. Technol. 142 (2016) 396.
[22] J.A. Kadijani, E. Narimani, Open J. Chem. Eng. Sci. 1 (2014) 79–86.
[23] F. Bernini, E. Castellini, D. Malferrari, M. Borsari, M.F. Brigatti, Microporous Mesoporous Mater. 211 (2015) 19–29.
[24] M.F. Brigatti, D. Malferrari, A. Laurora, C. Elmi, in: M.F. Brigatti, A. Mottana (Eds.), Layered Mineral Structures and Their Application in Advanced Technologies, EMU Notes in Mineralogy, 2011, pp. 1–71.
[25] F. Bernini, E. Castellini, D. Malferrari, G.R. Castro, C.I. Sainz-Díaz, M.F. Brigatti, M. Borsari, Appl. Mater. Interfaces 9 (2017) 1045–1056.
[26] R. Sui, S.K. Carefoot, C.B. Lavery, C.E. Deering, K.L. Lesage, N. Chou, C.J. Rose, R.A. Marriott, J. Mater. Chem. A 5 (2017) 9561–9671.
[27] R. Sui, K.L. Lesage, S.K. Carefoot, T. Fürstenhaupt, C.J. Rose, R.A. Marriott, Langmuir 32 (2016) 9197–9205.
[28] P. Yuan, H. He, F. Bergaya, D. Wu, Q. Zhou, J. Zhu, Microporous Mesoporous Mater. 88 (2006) 8–15.
[29] Z. Duan, R. Sun, R. Liu, C. Zhu, Energy Fuels 21 (2007) 2056–2065.
[30] M. Newville, J. Synchrotron Radiat. 8 (2001) 322–324.
[31] B. Ravel, M.J. Newville, J. Synchrotron Radiat. 12 (2005) 537–541.
[32] J.E. Plowman, T.M. Loehr, C.K. Schauer, O.P. Anderson, Inorg. Chem. 23 (1984) 3553–3559.
[33] W.R. McWhinnie, J.D. Miller, in: H.J. Hemeléus, A.G. Sharpe (Eds.), Advances in Inorganic Chemistry and Radiochemistry, Academic Press, New York, 1970, p. 163.
[34] A.A. Schilt, R.C. Tayor, J. Inorg. Nucl. Chem. 9 (1959) 211–221.
[35] J.E. Penner-Hahn, X-ray Absorption Spectroscopy. eLS, John Wiley & Sons, 2012.
[36] M.F. Brigatti, C.I. Sainz Diaz, M. Borsari, F. Bernini, E. Castellini, D. Malferrari, Rend. Fis. Acc. Lincei (2017) https://doi.org/10.1007/s12210-017-0615-1.
[37] V. Kunzl, Collection des Travaux Chimiques de Tchecoslovaquie 4 (1932) 213.
[38] M. Abuin, A. Serrano, J. Chaboy, M.A. Garcia, N. Carmona, J. Anal, Art Spectr. 28 (2013) 1118–1124.
[39] A. Boubnov, H. Lichtenberg, S. Mangold, J.D. Grunwaldt, J. Synchrotron Radiat. 22 (2015) 410–426.
[40] A. Davydov, K.T. Chuang, A.R. Sanger, J. Phys. Chem. B 102 (1998) 4745–4752.
[41] M.A. Montes-Morán, A. Concheso, C. Canals-Batlle, N.V. Aguirre, C.O. Ania, M.J. Martín, V. Masaguer, Environ. Sci. Technol. 46 (2012) 8992–8997.
[42] K.V. Stepova, D.J. Maquarrie, I.M. Krip, Appl. Clay Sci. 42 (2009) 625–628.
[43] T.J. Pinnavaia, Science 220 (1983) 365–371.
[44] S.M. Thomas, J.A. Bertrand, M.L. Occelli, F. Huggins, S.A. Gould, Inorg. Chem. 38 (1999) 2098–2105.
[45] D. Nguyen-Thanh, T.J. Bandosz, J. Phys. Chem. B 107 (2003) 5812–5817.
[46] D. Nguyen-Thanh, K. Block, T.J. Bandosz, Chemosphere 59 (2005) 343–353.
[47] K.V. Bineesh, D.R. Cho, S.Y. Kim, B.R. Jermy, D.W. Park, Catal. Commun. 9 (2008) 2040–2043.
[48] K.V. Bineesh, S.Y. Kim, B.R. Jermy, D.W. Park, J. Ind. Eng. Chem. 15 (2009) 207–211.
[49] K.V. Bineesh, D.K. Kim, D.W. Kim, H.J. Cho, D.W. Park, Energy Environ. Sci. 3 (2010) 302–310.
[50] K.V. Bineesh, S.Y. Kim, B.R. Jermy, D.W. Park, J. Mol. Catal. A 308 (2009) 150–158.
[51] K.V. Bineesh, D.K. Kim, H.J. Cho, D.W. Park, J. Ind. Eng. Chem. 16 (2010) 593–597.
[52] K.V. Bineesh, D.K. Kim, D.W. Park, Nanoscale 2 (2010) 1222–1228.
[53] K.V. Bineesh, M-il Kim, G.-H. Lee, M. Selvaraj, K. Hyun, D.W. Park, J. Ind. Eng. Chem. 18 (2012) 1845–1850.
[54] K.V. Bineesh, D.K. Kim, M.-I.L. Kim, M. Selvaraj, D.W. Park, Dalton Trans. 40 (2011) 3938–3945.
[55] K.V. Bineesh, M-il Kim, G.H. Lee, M. Selvaraj, D.W. Park, Appl. Clay Sci. 74 (2013) 127–134.
[56] M-il Kim, G.-H. Lee, D.-W. Kim, D.-H. Kang, D.-W. Park, J. Chem. Eng. 31 (2014) 2162–2169.
[57] R. KubebaTabase, D. Liu, A. Feilberg, Chemosphere 93 (2013) 1345–1351.
[58] S. Louhichi, A. Ghorbel, H. Chekir, N. Trabelsi, S. Khemakhem, Appl. Clay Sci. 127–128 (2016) 123–128.
[59] M. Mureddu, I. Ferino, A. Musinu, A. Ardu, E. Rombi, M.G. Cutrufello, P. Deiana, M. Fantauzzi, C. Cannas, J. Mater. Chem. A 2 (2014) 19396–19400.